



Research Paper

Plasmonic molybdenum oxide nanosheets supported silver nanocubes for enhanced near-infrared antibacterial activity: Synergism of photothermal effect, silver release and photocatalytic reactions



Qiaoqiao Yin^a, Linxiang Tan^a, Qingqing Lang^a, Xiaoxia Ke^a, Lijie Bai^a, Kaiyan Guo^a, Ru Qiao^{a,**}, Song Bai^{a,b,*}

^a Key Laboratory of the Ministry of Education for Advanced Catalysis Materials, College of Chemistry and Life Sciences, Zhejiang Normal University, Jinhua, Zhejiang, 321004, PR China

^b Hefei National Laboratory for Physical Sciences at the Microscale, School of Chemistry and Materials Science, University of Science and Technology of China, Hefei, Anhui, 230026, PR China

ARTICLE INFO

Keywords:

Near-infrared plasmonics
Antibacteria
Photothermal effect
Silver release
Photocatalysis

ABSTRACT

Plasmonic MoO_{3-x} nanosheets supported Ag nanocubes were designed as high-efficient Near-infrared (NIR) light driven antibacterial agent. The as-designed MoO_{3-x}-Ag not only significantly reduces the cost and toxicity of Ag, but also greatly enhances the antibacterial activity towards *E. coli* and *S. aureus* in comparison with bare MoO_{3-x} and Ag upon NIR laser irradiation. Three effects are believed to contribute to this enhancement: (1) the plasmonic MoO_{3-x}-Ag exhibits excellent NIR light absorption and photothermal conversion abilities, which help to kill bacteria; (2) NIR light induced heat in MoO_{3-x} also diffuses to Ag nanocubes and triggers the release of more Ag⁺, leading to bacterial cell death; (3) under NIR light irradiation, hot electrons and holes are generated and separated through MoO_{3-x}-Ag interface, which produces reactive species for the oxidation of out membrane of bacteria. The synergism of NIR light driven photothermal effect, silver release and photocatalytic reaction makes the designed plasmonic MoO_{3-x}-Ag a promising antibacterial agent for cleaning the microbial contaminated water environment.

1. Introduction

Utilization of solar energy for wastewater treatment and pathogenic bacteria killing represents an economic and clean approach to alleviating steadily worsening environmental issues and improving the public health [1–4]. Recently, various semiconductor-based photocatalysts have been developed to kill inactive bacteria under light irradiation [5–7]. However, one big limitation of the semiconductor-based photocatalysts is the contradiction between light absorption range and redox ability of photo-induced charge carriers [8,9]. Generally, wide bandgap semiconductors only absorb ultraviolet (UV) light (wavelength (λ) < 400 nm), which accounts for a very small fraction (\approx 5%) of solar spectrum. While for semiconductor with narrower bandgap, the light absorption extends to visible (400 < λ < 780 nm, \approx 43%) range, but the higher valence band maximum (VBM) or lower conductive band minimum (CBM) reduces the redox ability of the photogenerated charge carriers and decreases

the photocatalytic antibacterial activity. In comparison with UV and visible light, near-infrared (NIR) light (780 < λ < 2500 nm) not only accounts for a large proportion (\approx 52%) of the solar spectrum, but also penetrates into biological tissues more deeply with lower photo-damage to living bodies [10]. Thus the development of NIR responsive photocatalysts is a promising route to improving the solar energy conversion efficiency in bacteria killing with no observable damage to the exposed tissue [11].

Considering the bandgap of NIR light excitable semiconductor is too narrow to meet the energy requirement in driving the necessary redox reactions, alternative approaches have been utilized in the development of NIR light driven antibacterial photocatalysts. For one thing, upconversion nanocrystals can absorb low-energy NIR lights and emit high-energy UV or visible light in realizing the higher redox abilities [12,13]. However, upconversion nanocrystals can only absorb NIR light in a specific wavelength, greatly decreasing the utilization of solar photons. For another, noble metal nanocrystals with plasmonic absorption in NIR

* Corresponding authors at: Key Laboratory of the Ministry of Education for Advanced Catalysis Materials, College of Chemistry and Life Sciences, Zhejiang Normal University, Jinhua, Zhejiang, 321004, PR China.

** Corresponding author.

E-mail addresses: qiaoru@zjnu.cn (R. Qiao), songbai@zjnu.edu.cn (S. Bai).

<https://doi.org/10.1016/j.apcatb.2017.11.024>

Received 7 September 2017; Received in revised form 8 November 2017; Accepted 10 November 2017

Available online 11 November 2017

0926-3373/© 2017 Elsevier B.V. All rights reserved.

region generate hot charge carriers in driving the photocatalytic process for antibacterial application [14,15]. In comparison with upconversion nanocrystals, the plasmonic photocatalysts apparently enlarge the NIR light absorption range. Furthermore, the plasmonic photothermal effect can also help to kill the bacteria [16,17]. However, bare noble metal is uncompetitive for the future development of antibacterial agent considering the high cost and earth rarity of them. In addition, most of plasmonic noble metal absorb photons in the visible region, which can only be extended to the NIR range through precise shape control [8,15]. Moreover, noble metal also induces significant toxic effects to human health and environment [18]. Therefore, reducing the use of noble metals is a key issue in the future development of NIR responsive plasmonic photocatalytic antibacterial agents.

Recently, it was reported that plasmonic absorption has also been found on heavily doped semiconductor with an appreciable free carrier concentration, such as MoO_{3-x} and WO_{3-x} [19,20]. In comparison with plasmonic metal, plasmonic semiconductor greatly reduces the consumption of noble metal and decreases the toxicity to the organism [21]. Moreover, the plasmonic semiconductors show much stronger light absorption in the NIR region. In this paper, plasmonic MoO_{3-x} nanosheets were designed in combination with Ag nanocubes for effectively killing pathogenic bacteria under NIR light irradiation. MoO_{3-x} efficiently absorbs plasmonic light in NIR region, which not only converts to heat and kills the bacteria through photothermal lysis, but also transfers the heat to Ag and triggers the release of Ag^+ for an enhanced antibacterial activity. Furthermore, the hot electrons and holes can be generated and separated through MoO_{3-x} -Ag interface, which also generate free radicals and lead to the destruction of the outer membrane of the bacterial cell. Resulted from the synergistic effect of plasmonic heating, Ag^+ release and generated reactive species, both Gram-negative and Gram-positive bacteria were effectively killed by the designed MoO_{3-x} -Ag photocatalyst under NIR light irradiation. As far as we known, it is the first report on the development of plasmonic semiconductor based photocatalyst for NIR antibacterial application.

2. Experimental

2.1. Chemicals

Molybdenum powder (Aladdin, M109124), poly(vinyl pyrrolidone) (PVP, M.W. \approx 55000, Aldrich, 856568), NaSH (Sigma-Aldrich, 161527), ethylene glycol (EG, Sigma-Aldrich, 324558) and silver trifluoroacetate (Aladdin, S109509) were used in our synthesis. All other chemicals were of analytical grade and purchased from Sinopharm Chemical Reagent Co., Ltd. The water used in all experiments was de-ionized. All chemicals were used as received without further purification.

2.2. Synthesis of MoO_{3-x} nanosheets

In a typical synthesis [19], 2 mmol of molybdenum powder was added to 24 mL of ethanol in a 40 mL Teflon vessel. Then 3 mL of H_2O_2 was introduced and magnetically stirred for 1 h to obtain transparent yellow solution, which was then transferred to a Teflon-lined stainless-steel autoclave and heated at 150 °C for 12 h. After the autoclave had cooled down to room temperature, the resultant product was separated by centrifugation and washed with ethanol several times. The final product was then dried at 45 °C for 12 h.

2.3. Synthesis of Ag nanocubes

In a typical synthesis [22], 10 mL EG was added into a 50 mL three-neck flask and pre-heated under magnetic stirring at 150 °C. 0.12 mL NaSH (3 mM in EG) was quickly injected into the heated solution. After 2 min, 1 mL HCl solution (4 mM in EG) was introduced into the reaction solution, followed by the addition of 2.5 mL PVP solution (20 mg/mL in

EG) after another 2 min. Next, after the third 2 min, 0.8 mL solution of silver trifluoroacetate (282 mM in EG) was added. The reaction was allowed to proceed at 150 °C for 40 min. The product was collected by centrifugation, and washed with acetone and water several times to remove excess PVP. The as-obtained Ag nanocubes were redispersed in water for further use.

2.4. Preparation of MoO_{3-x} -Ag hybrid structures

In the synthesis of MoO_{3-x} -Ag structure, 10 mg MoO_{3-x} nanosheets were dispersed in 40 mL ethanol through sonication. Then 1.0 mL of Ag nanocubes (0.5 mg mL^{-1} in water) was added into the dispersion. The mixture was further sonicated for 5 min, and then transferred to a Teflon-lined stainless-steel autoclave, and heated at 100 °C for 1 h. After the autoclave had cooled down to room temperature, the resultant product was separated by centrifugation and washed with water several times. The final product was then dried at 45 °C for 12 h. Ag nanospheres were also assembled on the MoO_{3-x} nanosheets through the same method, which were obtained through etching Ag nanocubes with $\text{Fe}(\text{NO}_3)_3$ according to previous report [23].

2.5. Sample characterizations

Prior to electron microscopy characterizations, a drop of the aqueous suspension of particles was placed on a piece of carbon-coated copper grid and dried under ambient conditions. Transmission electron microscopy (TEM) and high-resolution TEM (HRTEM) images were taken on a JEOL JEM-2100F field-emission high-resolution transmission electron microscope operated at 200 kV. Scanning electron microscopy (SEM) was performed with a Hitachi S-4800 scanning electron microanalyzer with an accelerating voltage of 15 kV. Powder X-ray powder diffraction (XRD) patterns were recorded by using a Philips X'Pert Pro Super X-ray diffractometer with $\text{Cu-K}\alpha$ radiation ($\lambda = 1.5418 \text{ \AA}$). X-ray photoelectron spectra (XPS) were collected on an ESCALab 250 X-ray photoelectron spectrometer, using non-monochromatized $\text{Al-K}\alpha$ X-ray as the excitation source. UV-vis-NIR diffuse reflectance data were recorded in the spectral region of 240–1600 nm with a Shimadzu SolidSpec-3700 spectrophotometer. Photoluminescence (PL) spectra were recorded on a Jobin Yvon Horiba Fluorolog-3-Tau Spectrofluorometer. The concentrations of metal elements were measured as follows: the samples were dissolved with a mixture of HCl and HNO_3 (3:1, volume ratio) which was then diluted with 1% HNO_3 . The concentrations of metals were then measured with a Thermo Scientific PlasmaQuad 3 inductively-coupled plasma mass spectrometry (ICP-MS).

2.6. Cell cytotoxicity test

Cytotoxicity of the samples to human umbilical vein endothelial cells (HUVEC) was evaluated by a standard 3-(4,5-dimethylthiazol-2-yl)-2,5-diphenyl tetrazolium bromide (MTT) assay. HUVEC were seeded in 96-well U-bottom plates at a density of 5.0×10^4 – 1.0×10^5 cells per milliliter (90.0 μL per well) and cultured for 12 h in an incubator (37 °C, 5% CO_2), prior to the addition of the sample suspension at a range of concentrations (0 ~ 200 $\mu\text{g mL}^{-1}$). After being cultured for a further 24 h with samples, 20.0 μL of MTT solution (normal saline or 5.0 mg mL^{-1} phosphate buffer solution) was added into each sample, and incubated at 37 °C for 4 h. The culture media were discarded and then 150.0 μL of dimethylsulfoxide (DMSO) was added to each sample in order to dissolve the formazan, with shaking for at least 15 min. The corresponding spectra were recorded with a microplate reader at 595 nm. The cell viability rate (VR) was calculated based on the below equation:

$$\text{VR (\%)} = A/A_0 \times 100\%$$

where A is the absorbance of the experimental group (the cells treated with the sample suspensions) and A_0 is the absorbance of the control group.

2.7. Antibacterial activity measurement

S. aureus and *E. coli* were employed to study the antibacterial activities of the samples under the NIR irradiation (808 nm NIR laser, 0.5 W cm^{-2}). All materials and glassware were sterilized in an autoclave at 120°C for 30 min before use. The Luria–Bertani (LB) medium was prepared by mixing 10 g of tryptone, 5 g of yeast extract, and 10 g of NaCl in 1000 mL of deionized water. *E. coli* and *S. aureus* strains were cultured in LB nutrient broth at 37°C overnight. Each antibacterial test was carried out in a 20-mL sterilized glass bottle in which 10 mg of sample was mixed with 8 mL of the bacteria solution. After stirring under dark condition for 30 min, the bacteria solution was exposed to NIR irradiation for 10 min. After that, 200 μL of the bacteria suspension was taken out and spread on a nutrient agar petri dish, and then incubated on the petri dish at 37°C in dark for 24 h. In addition, 200 μL of suspended bacterial cells without the antibacterial agent served as a control was also spread on a nutrient agar plate. The number of surviving colonies for each plate was counted. To investigate the main reactive species generated from $\text{MoO}_{3-x}\text{-Ag}$, 10 mM ethylene diamine tetraacetic acid (EDTA, 10 mM), 10 mM potassium bromate (KBrO_3 , 10 mM) and 10 mM tertiary butanol (*t*-BuOH, 10 mM) were used as scavengers for h^+ , $\cdot\text{O}_2^-$ and $\cdot\text{OH}$ in the reaction system, respectively. Simultaneously, 1.5 mL of each scavenger was added into the sterilized glass bottle, the following experimental processes were the same as those of the antibacterial experiment. Total organic carbon (TOC) concentration during the antibacterial process was carried out on a Shimadzu TOC-VSCH analyzer in the solutions with different irradiation times. During the stability test, the antibacterial experiment was circularly conducted for six times. After each photocatalytic antibacterial cycle, the used photocatalyst was collected by centrifuging and washing with water for next cycle.

2.8. Photothermal effect measurement

To examine the photothermal effect induced by NIR irradiation, 1.5 mL of 2 mg mL^{-1} Ag nanocubes, MoO_{3-x} nanosheets, and $\text{MoO}_{3-x}\text{-Ag}$ dispersions were irradiated for 10 min by a NIR laser (808 nm , 0.5 W cm^{-2}), respectively. The temperature changes of the solutions were monitored using a submerged thermocouple microprobe.

2.9. Silver release measurement

The sample suspensions placed in a 96-well plate were subjected to NIR laser irradiation (808 nm , 0.5 W cm^{-2}) for 10 min. The irradiated solutions were then collected and centrifuged to obtain the supernatant. The suspensions of samples without NIR laser irradiation were used as the contrast experiment. The released Ag^+ concentration was determined by a Thermo Scientific PlasmaQuad 3 inductively-coupled plasma mass spectrometry (ICP-MS).

2.10. Photoelectrochemical measurement

4.0 mg as-synthesized products were dispersed in 1-mL ethanol, which were then uniformly spin-dropped onto a $2.5 \text{ cm} \times 2.5 \text{ cm}$ indium tin oxide (ITO)-coated glass by a spin coater (SC-1B, China). Subsequently, the ITO-coated glass was heated at 80°C in a vacuum oven for 1 h. The photocurrents were measured on a CHI 660D electrochemical station (Shanghai Chenhua, China) in ambient conditions under irradiation of a 300-W Xe lamp (Solaredge 700, China). NIR light was used as the illumination source, which was realized by using a 780-nm cutoff filter (long-wave-pass). Standard three-electrode setup was used with the ITO coated glass as photoelectrode, a Pt foil as counter

electrode, and a Ag/AgCl electrode as reference electrode. The three electrodes were inserted in a quartz cell filled with $0.5\text{-M Na}_2\text{SO}_4$ electrolyte. The photoresponse of the prepared photoelectrodes (i.e., *I-t*) was operated by measuring the photocurrent densities under chopped light irradiation (light on/off cycles: 60 s) at a bias potential of 0 V vs. Ag/AgCl for 400 s.

2.11. Photocatalytic activity measurement

Photocatalytic activities of the samples were evaluated by the degradation of rhodamine B (RhB) solution. In a typical process, 5 mg of as-prepared products were added into 10 mL RhB ($2 \times 10^{-5} \text{ M}$) in a 50-mL breaker. Then, the suspensions were stirred for 12 h in dark before reaching an adsorption-desorption equilibrium between the samples and RhB molecules. Subsequently, the suspensions were divided into 20 equal parts and added into a 96-well plate. The plates were then subjected to NIR laser irradiation (808 nm , 0.5 W cm^{-2}) to perform the photocatalytic reaction. At given time intervals (30 min), 200 μL of the suspension in each well were intermittently collected to measure the concentration of RhB by UV-vis absorption spectroscopy (Shimadzu UV-2450).

2.12. Oxygen species and H_2O_2 measurement

To determine the involved oxygen radicals, the mixture dispersion of $\text{MoO}_{3-x}\text{-Ag}$ (100 μL , 4 mg/mL) with trapping molecules (100 μL , 50 mM) in water or methanol were characterized with a JES-FA200 electron spin resonance (ESR) spectrometer at 20°C . The measurements were performed in incident light and dark conditions, respectively. The H_2O_2 involved in the reaction is detected through a colorimetric titration method according to previous report [24].

3. Results and discussion

3.1. Sample synthesis and characterization

In the design, MoO_{3-x} nanosheets were firstly synthesized through a solvothermal method according to the previous report [19]. The edge length of as-prepared MoO_{3-x} nanosheets is larger than 300 nm, while the average thickness is below 20 nm (Fig. S1). According to the size of the nanosheets, the area percentage of the top and bottom flat surface is over 95%. The large flat surface facilitates the loading of other components in forming the hybrid structures with large contact area for interfacial charge transfer, while the low thickness shortens the distance of charge transfer in the bulk MoO_{3-x} , reducing the possibility of charge carrier loss. On the other hand, Ag nanocubes with edge length of ca. 50 nm were also synthesized in fabricating the hybridized photocatalytic antibacterial agent (Fig. S2). The cubic profile of Ag nanocrystals ensures the face-to-face contact with the nanosheet structure of MoO_{3-x} for high-efficient interfacial charge transfer.

The Ag nanocubes were then deposited on MoO_{3-x} nanosheets to form a $\text{MoO}_{3-x}\text{-Ag}$ hybrid nanostructure through an solvothermal self-assembly method (Fig. 1a). As shown in Fig. 1b and c, cubic Ag nanocrystals are uniformly distributed over the flat surface of MoO_{3-x} nanosheets. Bare MoO_{3-x} nanosheets and Ag nanocubes can be rarely seen in the TEM images, confirming the stronger interaction between them. In the as-obtained $\text{MoO}_{3-x}\text{-Ag}$ hybrid structure, MoO_{3-x} nanosheets are combined with Ag nanocubes through facet-to-facet contact, which can be clearly resolved by a cross-section TEM image with a standing-up MoO_{3-x} nanosheet (Fig. S3). HRTEM image in Fig. 1d indicates that both MoO_{3-x} nanosheets and Ag nanocubes are monocrystalline structures. The flat surface of the MoO_{3-x} nanosheets is covered by (111) faces, while the Ag nanocubes are enclosed by (100) planes. As a result, $\text{MoO}_{3-x}(111)\text{-Ag}(100)$ interfaces are formed between them. Electrostatic interaction may be the driving force in connection between MoO_{3-x} and Ag. Based on Zeta potential measurement,

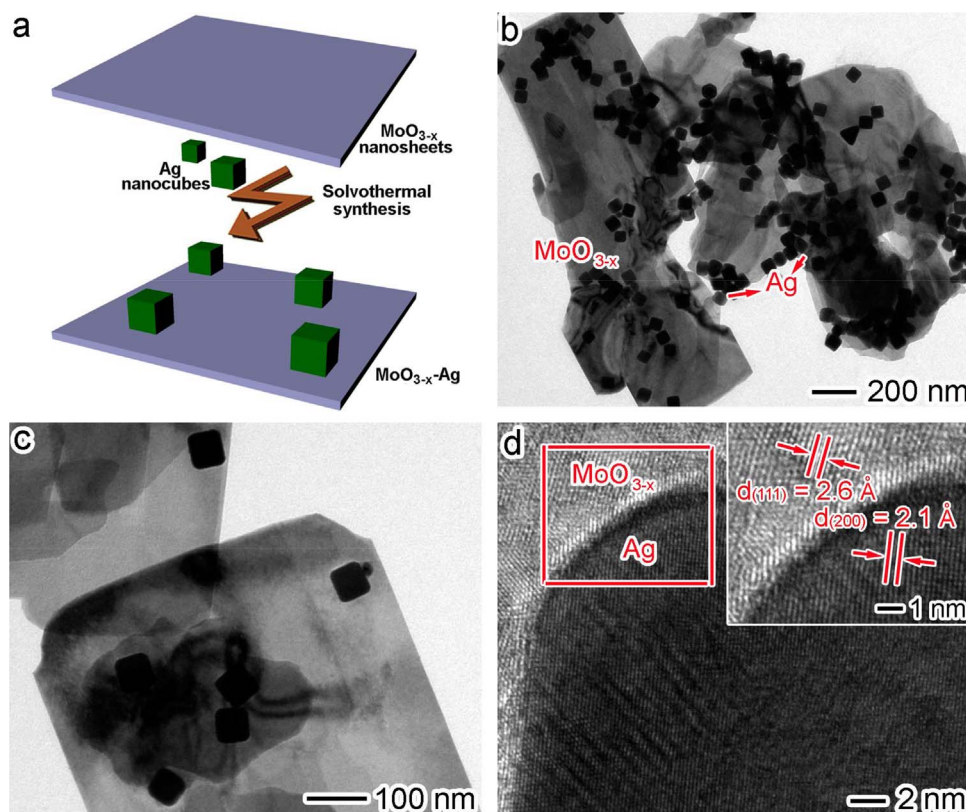


Fig. 1. (a) Schematic illustrating the synthesis of the MoO_{3-x}-Ag hybrid structure, (b,c) TEM and (d) HRTEM images of MoO_{3-x}-Ag hybrid structure.

MoO_{3-x} nanosheets possess positive charged flat surface, which may be resulted from the large amount of O²⁻ vacancies, while the surface of Ag nanocubes is negative charged owing to PVP capping agent has an easily polarized functional group “-C=O”, in which repeated unit “O” has a negative charge [25].

The structure of as-obtained MoO_{3-x}-Ag hybrid structure is characterized by X-ray powder diffraction (XRD) pattern with bare MoO_{3-x} and Ag as reference samples. As shown in Fig. 2a, all the peaks of MoO_{3-x} match well with orthorhombic phase MoO₃ (JCPDS 05-0508), while the peaks of Ag nanocubes are assigned to the face-centered cubic (fcc) Ag (JCPDS 87-0597). As for the XRD pattern of MoO_{3-x}-Ag, both the peaks of MoO₃ and Ag are shown, further confirming the combination of them. UV-vis-NIR absorption spectra of bare Ag, MoO_{3-x} and MoO_{3-x}-Ag were shown in Fig. 2b. Ag nanocubes exhibit a light absorption in the range of 400–500 nm (suspension in yellow color, Fig. S4a), corresponding to their plasmonic band in the visible region [26]. As for the absorption spectrum of MoO_{3-x}, a light absorption in the UV region with the absorption edge at about 420 nm corresponds to the wide bandgap of MoO₃, while a much stronger light absorption in the range of 420–1600 nm is attributed to the plasmonic absorption of MoO_{3-x} (suspension in blue color, Fig. S4b). Resulted from the strong plasmonic absorption of MoO_{3-x}, the light absorption ability of MoO_{3-x}-Ag (suspension in grey blue color, Fig. S4c) is comparable in comparison with that of MoO_{3-x} in the NIR region. The only difference between them is the additional visible light (400 < λ < 500 nm) absorption in the MoO_{3-x}-Ag sample resulted from the plasmonic band of Ag nanocubes. Furthermore, it should be noted that the difference between the absorption spectra of MoO_{3-x} and MoO_{3-x}-Ag in the longer wavelength (980 < λ < 1600 nm) is attributed to the scattering of Ag nanocubes on the surface of MoO_{3-x} nanosheets [27].

The chemical composition of as-obtained MoO_{3-x}-Ag sample was characterized by XPS spectra. The survey XPS spectrum indicates the Mo, Ag and O elements in the MoO_{3-x}-Ag (Fig. S5). In the high-resolution spectrum of Mo3d (Fig. 2c), the binding energies of 231.7 eV (Mo3d_{5/2}) and 234.8 eV (Mo3d_{3/2}) are assigned to Mo⁵⁺, while the

peak centered at 233.1 eV (Mo3d_{5/2}) and 236.3 eV (Mo3d_{3/2}) corresponds to Mo⁶⁺, indicating the formation of MoO_{3-x}. According to the XPS peak area of Mo3d, the Mo⁵⁺ accounts for 70.2% of the total Mo states, revealing the large amount of oxygen vacancies in the MoO_{3-x}. In the high-resolution Ag3d spectrum (Fig. 2d), the binding energies of 368.3 eV (Ag3d_{5/2}) and 374.3 eV (Ag3d_{3/2}) are in good agreement with the zero valence of Ag. Through the ICP-MS measurement, the loading amount of Ag in the MoO_{3-x}-Ag sample was determined to be 4.76 wt.%.

3.2. in vitro cytotoxicity study and antibacterial performance

Before the as-synthesized MoO_{3-x}-Ag hybrid nanostructure was used for antibacterial therapy, its potential toxicity to host cells was evaluated by using bare MoO_{3-x} nanosheets and Ag nanocubes as reference samples. The standard MTT assay was performed to examine the cytotoxicity of them to HUVEC. As shown in Fig. 3, Ag nanocubes are highly toxic to the cell. When the concentration of Ag is only 5 μg mL⁻¹, the cell viability has been decreased to around 54.4%. In contrast, MoO_{3-x} nanosheets are almost nontoxic to HUVEC. Even after exposure to the high concentration MoO_{3-x} (50 μg mL⁻¹), the cells still have a high survival rate (more than 88.6%). With the further combination of MoO_{3-x} and Ag, the cytotoxicity of MoO_{3-x}-Ag is greatly decreased resulted from the low content of highly toxic Ag in the sample. When the concentration of MoO_{3-x}-Ag is in the range of 0–25 μg mL⁻¹, more than 84% cells are survived. The low toxicity makes the MoO_{3-x}-Ag a potential antibacterial material in the following study.

The antibacterial activities of Ag, MoO_{3-x} and MoO_{3-x}-Ag against Gram-negative and Gram-positive bacteria were then investigated using *E. coli* and *S. aureus* as model bacteria, respectively. As shown in Fig. 4, NIR laser alone does not kill bacteria effectively, and the viabilities of both *E. coli* and *S. aureus* are more than 96.7%. After incubation with MoO_{3-x}-Ag without irradiation, the bacterial viabilities reach to 88.4% for *E. coli* and 90.8% for *S. aureus*, respectively, much approximate to the values of bare Ag (92.9% for *E. coli* and 90.8% for *S. aureus*) and

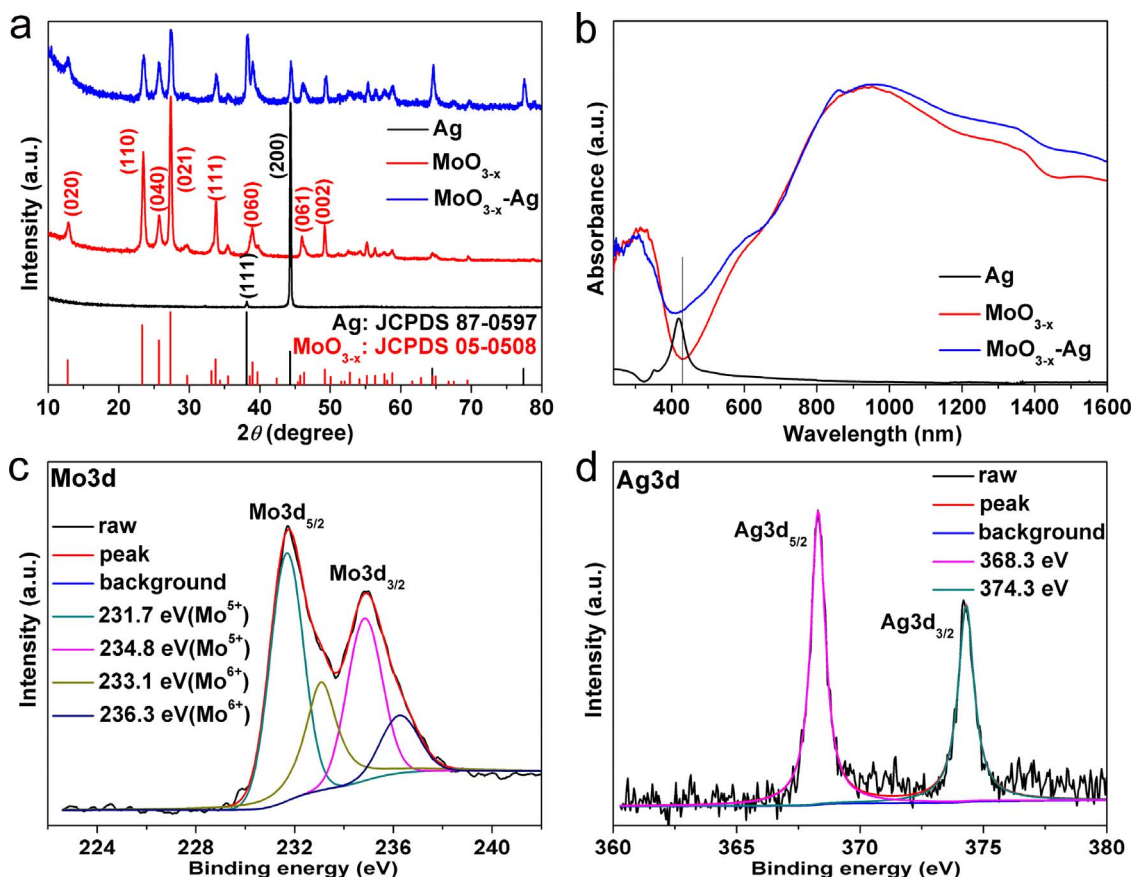


Fig. 2. (a) XRD patterns of bare Ag, MoO_{3-x} and MoO_{3-x}-Ag, (b) UV-vis-NIR absorption spectra of Ag, MoO_{3-x} and MoO_{3-x}-Ag, (c,d) high-resolution XPS spectra of MoO_{3-x}-Ag hybrid structure: (c) Mo3d and (d) Ag3d.

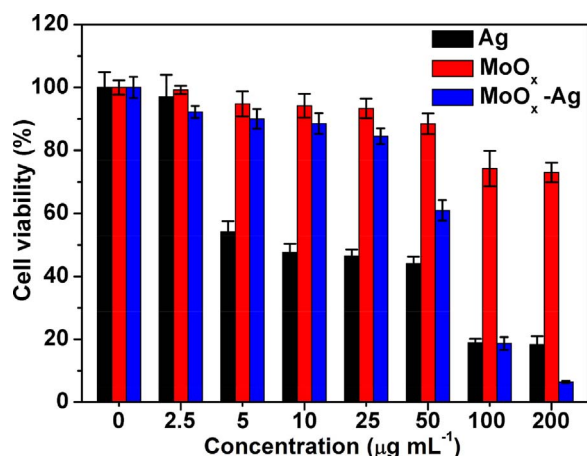


Fig. 3. The cytotoxicity of different concentrations of bare Ag, MoO_{3-x} and MoO_{3-x}-Ag to HUVEC.

MoO_{3-x} (94.8% for *E. coli* and 93.5% for *S. aureus*). Interestingly, when both bacteria were treated with MoO_{3-x}-Ag upon NIR laser irradiation, 99.2% of *E. coli* and 97.0% of *S. aureus* are killed, much more than those of Ag (13.6% of *E. coli* and 10.7% of *S. aureus*) and MoO_{3-x} (23.6% of *E. coli* and 14.7% of *S. aureus*) under the same experimental conditions, confirming the synergistic effect between MoO_{3-x} and Ag for the enhanced antibacterial activity under NIR laser irradiation.

In addition to the antibacterial activity, antibacterial durability of MoO_{3-x}-Ag is also investigated through six successive cycles. The antibacterial durability results of *E. coli* and *S. aureus* were provided in Fig. S6a and b, respectively. It can be found that the antibacterial activity

gradually decreases with the increase of the cycle number. The anti-microbial rate remains only 30.3% for *E. coli* and 43.2% *S. aureus* after six cycles, indicating the low reusability of MoO_{3-x}-Ag. From the TEM images of MoO_{3-x}-Ag after the photocatalytic cycles (Fig. S6c and d), it can be clearly seen that though there is only a trace amount of Ag nanocrystals detached from MoO_{3-x} nanosheets, the shape of Ag nanocrystals has been changed into irregular nanospheres for both *E. coli* and *S. aureus* resulted from the release of Ag⁺. After the antibacterial cycles, Ag contents in the MoO_{3-x}-Ag were measured to be 3.86 wt.% (for *E. coli*) and 4.12 wt.% (for *S. aureus*), much lower than that before the cycles.

SEM images of *E. coli* and *S. aureus* before and after incubated with MoO_{3-x}-Ag under NIR irradiation are provided in Fig. 5. It can be clearly seen that the untreated *E. coli* and *S. aureus* are intact with smooth surface. After incubated with MoO_{3-x}-Ag, the cell walls are wrinkled and damaged, revealing the antibacterial activity was achieved by damaging the cell walls of the bacteria. TOC during the antibiosis experiment was investigated to examine the level of organic carbon dissolved from *E. coli* and *S. aureus* with MoO_{3-x}-Ag as antibacterial agent. For both bacteria, with the extension of illumination time, TOC firstly increases and then decreases in the reaction solution (Fig. S7). The possible reason is that the disruption of bacteria results in the decomposition of macromolecular components and the transfer of carbon from solid phase to liquid phase, corresponding to the increase in TOC. Then the continuous illumination further transfer the carbon to gas phase by mineralizing into CO₂, leading to the decrease of TOC [28]. To further exclude the self-recovery function of bacteria, the colonies of *E. coli* and *S. aureus* killed by MoO_{3-x}-Ag in the nutrient agar petri dish were stood for 24 h at room temperature. It was found that there is no increase in the cell viability for both bacteria, indicating that the killed bacteria can not recover themselves (Fig. S8).

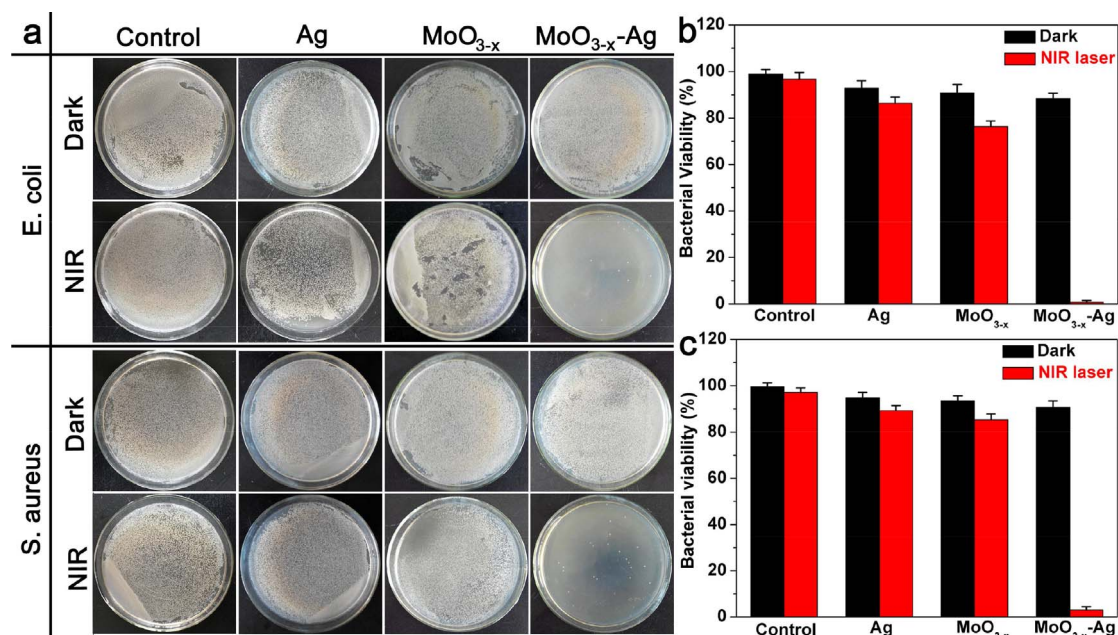


Fig. 4. (a) Photographs of colonies of *E. coli* (top) and *S. aureus* (bottom) treated with Ag, MoO_{3-x} and $\text{MoO}_{3-x}\text{-Ag}$ without and with NIR laser irradiation, respectively; (b,c) histograms of (b) *E. coli* and (c) *S. aureus* viability. The concentrations of Ag, MoO_{3-x} and $\text{MoO}_{3-x}\text{-Ag}$ are 0.0625, 1.125 and 1.125 mg mL^{-1} for both of *E. coli* and *S. aureus*, respectively.

3.3. Photothermal effect and NIR-triggered silver release

To further investigate the mechanism of the enhanced antibacterial activity of $\text{MoO}_{3-x}\text{-Ag}$, the photothermal effect in converting light into heat was studied firstly, which are widely investigated in the plasmonic-driven photocatalytic antibacterial reactions [17,21]. To perform the investigation, Ag (2 mg mL^{-1}), MoO_{3-x} (2 mg mL^{-1}) and $\text{MoO}_{3-x}\text{-Ag}$ (2 mg mL^{-1}) aqueous suspensions were exposed to 808 nm laser at a powder density of 0.5 W cm^{-2} for 10 min. As illustrated in

Fig. 6a, MoO_{3-x} nanosheets show a temperature increase up by 21.5°C , much larger than that of Ag nanocubes (15.9°C). Since only the MoO_{3-x} shows a plasmonic absorption in the wavelength of 808 nm, the laser energy can be more efficiently transformed to heat by MoO_{3-x} than Ag [21,29]. Moreover, a further elevated temperature was realized by $\text{MoO}_{3-x}\text{-Ag}$, confirming the combination of MoO_{3-x} and Ag results in the enhancement in the photothermal conversion capability. The possible reason is that the heat generated by MoO_{3-x} nanosheets can be effectively diffused to Ag nanocubes through the interface between them.

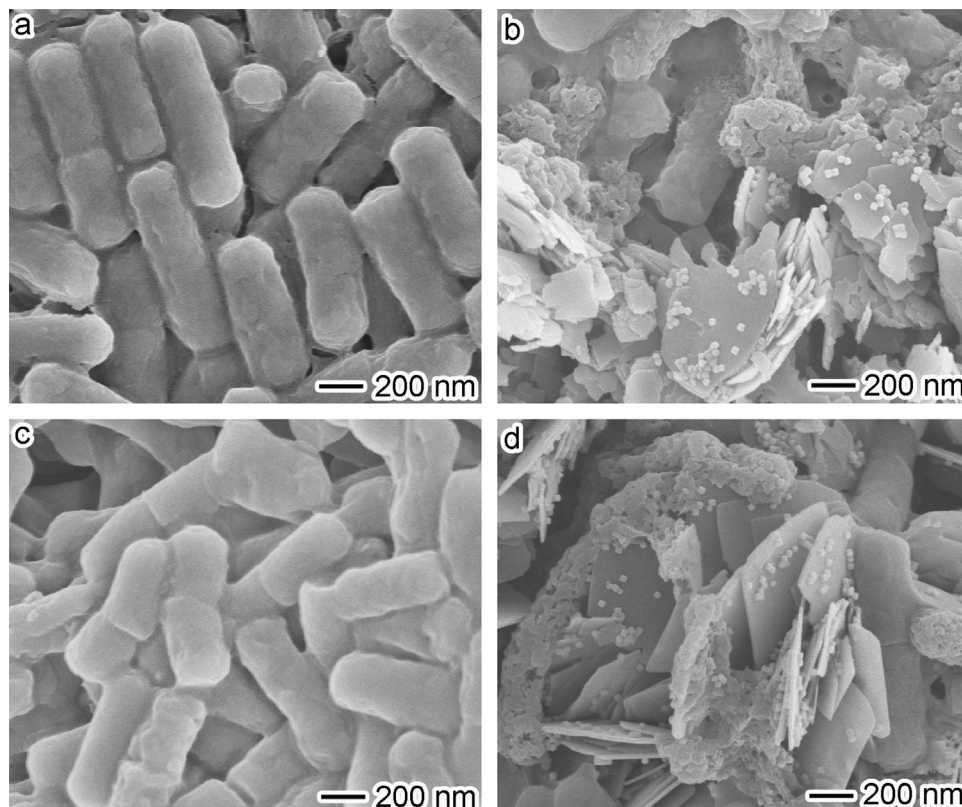


Fig. 5. SEM images of (a,b) *E. coli* and (c,d) *S. aureus* before and after incubated with $\text{MoO}_{3-x}\text{-Ag}$ under NIR irradiation, respectively.

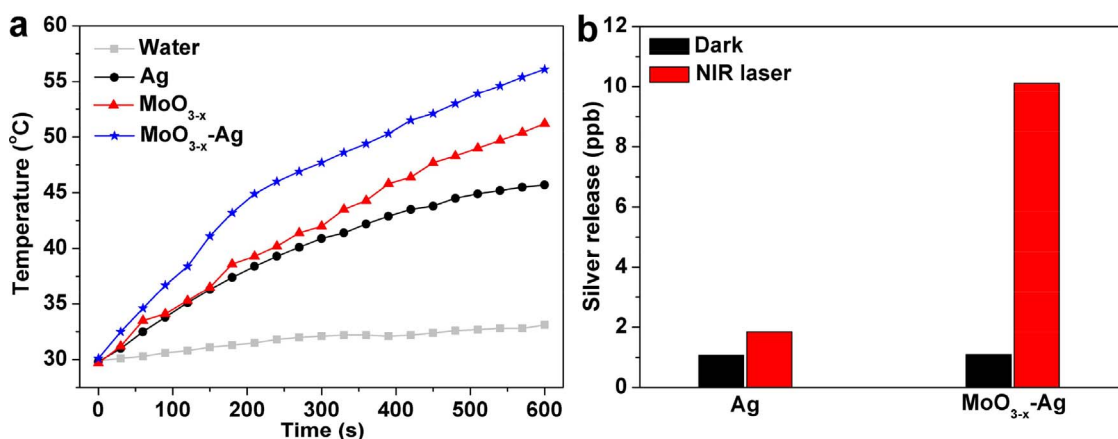


Fig. 6. (a) Temperature *versus* time plots recorded for Ag, MoO_{3-x} and MoO_{3-x}-Ag suspension upon irradiation by a 0.5 W cm⁻² 808 nm NIR laser; (b) silver released from 0.5 and 1.8 ppm of Ag and MoO_{3-x}-Ag (containing 0.09 mg mL⁻¹ Ag) with and without NIR laser (0.5 W cm⁻² 808 nm) irradiation.

Then the excellent thermal conductivity and low heat capacity of Ag nanocubes accelerate the rise of temperature. It should be noted that pure water displays a negligible change in temperature under the same irradiation conditions. Considering high temperature results in the protein denaturation of bacteria and loss of enzyme activity, the as-prepared MoO_{3-x}-Ag with excellent photothermal capability effectively inhibits the cell growth of bacteria through releasing sufficient heat.

Moreover, it has been reported that Ag⁺ can easily accumulate around the living bacterial cells and strongly bind to thiol group (SH) found in enzymes and proteins on the cellular surface, which interferes with cell division and leads to bacterial cell death [30]. To take this in consideration, the silver releases from the Ag and MoO_{3-x}-Ag samples with and without NIR irradiation were characterized by ICP-MS. As shown in Fig. 6b, the release amounts of Ag⁺ from bare Ag under NIR laser irradiation (0.5 W cm⁻², 808 nm) is much similar to that in the dark. However, as for the MoO_{3-x}-Ag, the release amounts of Ag⁺ are highly dependent on whether the samples were subjected to NIR irradiation. 10 min NIR irradiation of the MoO_{3-x}-Ag leads to an increase of the release amount of Ag⁺ by 5.5 times, in comparison with the non-irradiated control. It has been reported that silver release is a co-operative oxidation process requiring both dissolved dioxygen and protons with oxygen reduction to superoxide anion through electron reaction, which further reacts with Ag to release Ag⁺ with the reason that H₂O₂ is a more powerful oxidant than O₂ (2H⁺ + O₂ + 2e⁻ → H₂O₂; H₂O₂ + 2H⁺ + 2Ag → 2Ag⁺ + 2H₂O) [31]. Both the MoO_{3-x} and NIR irradiation can not change the silver release mechanism on the Ag nanocubes. Nevertheless, it has been reported that the rate of silver release was also dependent on the temperature [29]. When illuminated with NIR laser, the photothermal effect of MoO_{3-x}-Ag gives rise to the rapid increase in the surface temperature of supported Ag nanocubes, which may trigger the fast release of silver. To confirm this, release amounts of Ag⁺ from bare Ag nanocubes at different temperatures were measured (Fig. S9), in which more released Ag⁺ were determined at the higher temperature, indicating the photothermal effect of MoO_{3-x}-Ag accelerates the Ag⁺ release and further enhances the antibacterial activity.

3.4. Charge kinetics and photocatalytic performance

In addition to the antibacterial mechanisms of NIR-triggered photothermal effect and Ag⁺ release, it has also been reported that the photogenerated free radicals can also penetrate the cell wall and lead to bacterial death by oxidation through photocatalytic process [31,32]. In view that the photocatalytic activity is greatly determined by the generation and transfer of photogenerated charge carriers, the charge kinetics of the samples were investigated prior to the photocatalytic performance measurements. As shown in Fig. 7a, under NIR light

irradiation, MoO_{3-x}-Ag exhibits a much higher photocurrent response in comparison with bare Ag and MoO_{3-x}, indicating an obvious charge transfer between MoO_{3-x} and Ag. Considering only MoO_{3-x} is excited by the NIR light, the charge carriers can only be generated in MoO_{3-x} and then transferred to Ag nanocubes through MoO_{3-x}-Ag interface. Furthermore, considering the absorption edge of bare MoO_{3-x} is in the UV region (Fig. 2a). The photogenerated charge carriers are not resulted from the excitation of electrons from conduction band (CB) to valence band (VB) with the reason that the energy of NIR photons can not match with the wide bandgap of MoO_{3-x}. Alternatively, the incident NIR photons are absorbed by the free electrons in plasmonic MoO_{3-x}, and the electrons leap over the Fermi level to a higher energy level and form hot electrons [33,34]. Leaving hot holes in the MoO_{3-x}, the hot electrons then transfer to highly conductive Ag nanocubes in realizing the spatial separation of hot electrons and holes [35,36]. Resulted from the hot electrons transfer on the MoO_{3-x}-Ag interface, spatial separation of hot electrons and holes were realized. Then the separated electrons and holes may participate in the formation of free radicals in realizing the enhanced photocatalytic activity of MoO_{3-x}-Ag. To confirm this, photocatalytic degradation of RhB was measured as a model reaction under NIR laser irradiation. As shown in Fig. 7b, MoO_{3-x}-Ag actually exhibits significantly superior photocatalytic activity in the degradation of RhB in comparison with bare MoO_{3-x} and Ag.

To further elucidate the relationship between the enhanced photocatalytic activity and the improved antibacterial performance of MoO_{3-x}-Ag, the active species involved in the antibacterial process are identified by the free radical trapping experiment. Ethylenediaminetetraacetic acid (EDTA), potassium bromate (KBrO₃) and tertiary butanol (t-BuOH) were used as scavengers to detect the hole (h⁺), superoxide radical (O₂^{•-}) and hydroxyl radical (•OH), respectively. Also bacteria without treatment of any scavengers were also performed as control experiment. As shown in Fig. 7c, compared with that of no scavenger, the disinfection efficiency of MoO_{3-x}-Ag significantly decreases after the addition of EDTA, suggesting the h⁺ is the crucial reactive species during the photocatalytic antibacterial process. Besides, the inhibition of photocatalytic antibacterial activity also occurs in the presence of KBrO₃ and t-BuOH though the inhibition efficiency is much lower than that EDTA, suggesting that the O₂^{•-} and •OH species also play a role in the antibacterial process. To further exclude the cytotoxicity of scavengers during the trapping experiment, comparative experiment was performed under the same conditions as the trapping experiment except the absence of antibacterial agent. During the NIR laser irradiation, it was found that there was no obvious difference in the bacterial colonies for each scavenger, indicating the low cytotoxicity of the scavengers to bacteria (Fig. S10).

The formed oxygen radicals were examined using 5,5-dimethyl-1-pyrroline-N-oxide (DMPO) as a trapping agent. The ESR spectra of

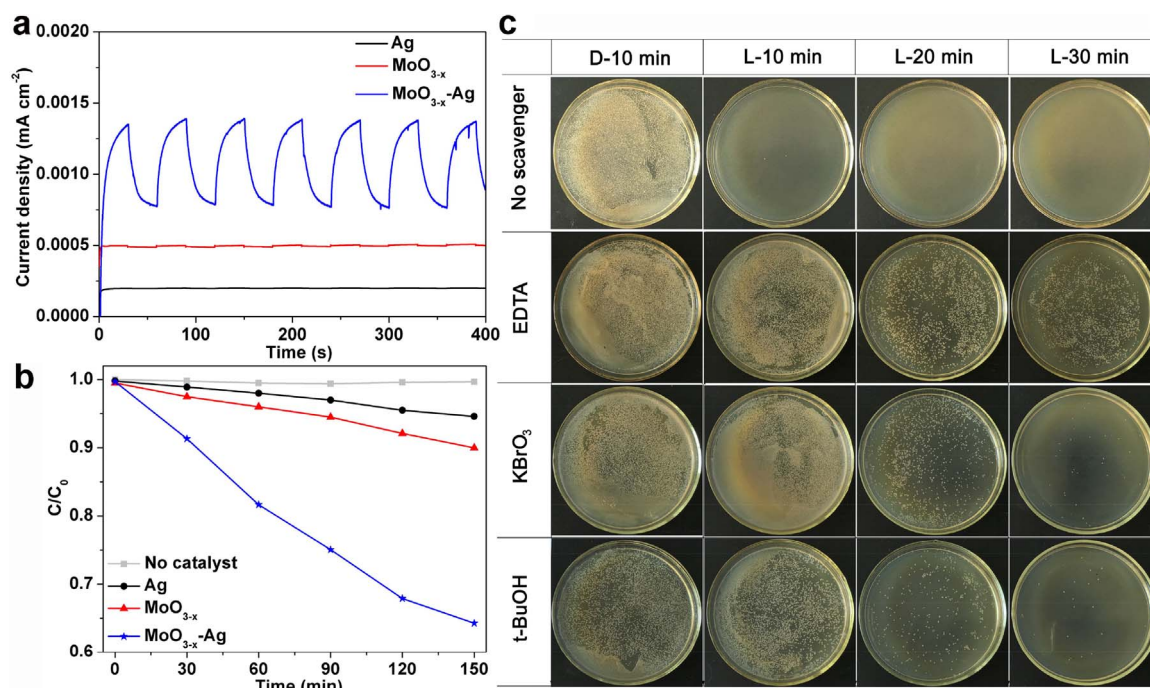


Fig. 7. (a) Photocurrent vs. time (*I-t*) curves of Ag, MoO_{3-x} and MoO_{3-x}-Ag under NIR light irradiation; (b) photocatalytic activities of Ag, MoO_{3-x} and MoO_{3-x}-Ag in the degradation of RhB under NIR laser irradiation; (c) photographs of colonies of *Bacillus subtilis* treated with MoO_{3-x}-Ag under NIR laser irradiation in the presence of different scavengers.

MoO_{3-x}-Ag after mixing DMPO in methanol and water dispersion were provided in Fig. S11a and b, respectively. Under NIR irradiation in methanol and H₂O, ESR signals with intensity ratio of 1:1:1:1 and 1:2:2:1 are clearly displayed for the MoO_{3-x}-Ag, which are the characteristics for O₂^{•-} and [•]OH radicals, respectively [37,38]. While no signal is detected in dark, verifying that the hydroxyl and superoxide radicals are produced in the photocatalytic process. It is worth noting that the signal of DMPO degradation with 1:1:1 characteristic intensity has also been observed for the MoO_{3-x}-Ag in both water and methanol under NIR light irradiation, which is ascribed to the production of singlet oxygen [39]. Furthermore, the H₂O₂ intermediate in the reaction can also be detected through a colorimetric titration method under acidic reaction conditions, in which a yellow colored Ti(IV)-H₂O₂ complex is formed and exhibits a characteristic absorption peak at λ = 410 nm (Fig. S11c) [40]. This result is in accordance with the previous report on the antibacterial photocatalysts, in which h⁺ could react with adsorbed hydroxyl groups (OH⁻) on the surface of bacteria and produce surface adsorbed [•]OH and H₂O₂, which could oxidize the out membrane of bacteria [41,42]. In the meantime, O₂^{•-} originated from electrons (e⁻) also participates in the antibacterial reaction. According to the photocatalytic mechanism of MoO_{3-x}-Ag, it can be concluded that the remnant hot holes on the surface of MoO_{3-x} are the most important reactive species during the photocatalytic antibacterial process. Of course, MoO_{3-x} is partially oxidized by the holes left on the MoO_{3-x} nanosheets, which can be confirmed by the UV-vis-NIR spectra and photo images of MoO_{3-x}-Ag before and after the antibacterial cycles (Fig. S12). For both of *E. coli* and *S. aureus*, after the photocatalytic antibacterial process, there is a decrease in the plasmonic absorption of MoO_{3-x} in the range of 700–1400 nm. And the grey blue color of MoO_{3-x}-Ag becomes lighter, corresponding to the decrease in the number of oxygen vacancies, which is another reason for the reduced antibacterial activity in the cyclic process.

It should be noted that the shape of Ag on MoO_{3-x} nanosheets greatly determine the antibacterial activity with the reason that the facet-to-facet contact between Ag nanocubes and MoO_{3-x} nanosheet is the key to achieving efficient charge transfer. For comparison, Ag nanospheres were also assembled on the MoO_{3-x} nanosheets to form a new

MoO_{3-x}-Ag hybrid structure (namely MoO_{3-x}-Ag NSs) through the same synthetic method (Fig. S13a). According to the photocurrent results (Fig. S13b), the electron transfer efficiency from MoO_{3-x} nanosheets to Ag nanospheres is much lower in comparison with that from MoO_{3-x} nanosheets to Ag nanocubes. As illustrated by Fig. S13c, the interfacial contact area between MoO_{3-x} nanosheets and Ag nanospheres is much smaller in comparison with that between nanosheets and nanocubes, which not only decreases the stability of Ag on MoO_{3-x} nanosheets, but also leads to inefficient charge and heat transfer in reducing the photocatalytic activity. As a result, MoO_{3-x} supported Ag nanospheres structure exhibits obviously weaker antibacterial activity than MoO_{3-x} supported Ag nanocubes structure (namely MoO_{3-x}-Ag NCs) (Fig. S13d).

According to the above results, three effects are believed to contribute to the enhanced antibacterial activity of the designed MoO_{3-x}-Ag driven by NIR light irradiation. As shown in Fig. 8, with the NIR irradiation of MoO_{3-x}-Ag, the plasmonic MoO_{3-x} nanosheets not only generate heat through photothermal effect, but also produce hot charge carriers. Both of the heat and hot electrons then transfer to Ag nanocubes through MoO_{3-x}-Ag interface, resulting in the elevated temperature as well as separation of electrons and holes, respectively. On one hand, the elevated temperature not only results in the protein denaturation and loss of enzyme activity in inhibiting the cell growth of bacteria, but also triggers the release of more Ag⁺. Ag⁺ accumulates around the living bacterial cells and strongly binds to thiol group (SH) found in enzymes and proteins on the cellular surface, which interferes with cell division and leads to bacterial cell death. On the other hand, the separated electrons and holes also convert to reactive species, which penetrate the cell wall and lead to bacterial death by oxidation through photocatalytic process. Thus the improved NIR antibacterial performance of the MoO_{3-x}-Ag is resulted from the synergistic effect of photothermal effect, Ag⁺ release and free radical reaction. The photocatalytic mechanism and role between the three effects and bacteria are also illustrated in Fig. S14. In comparison with the difference in the photothermal effect and silver release between different samples, the difference in the antibacterial activity appears to be significantly larger, indicating that the photocatalytic reaction may make a major contribution to the enhanced antibacterial activity of MoO_{3-x}-Ag. For

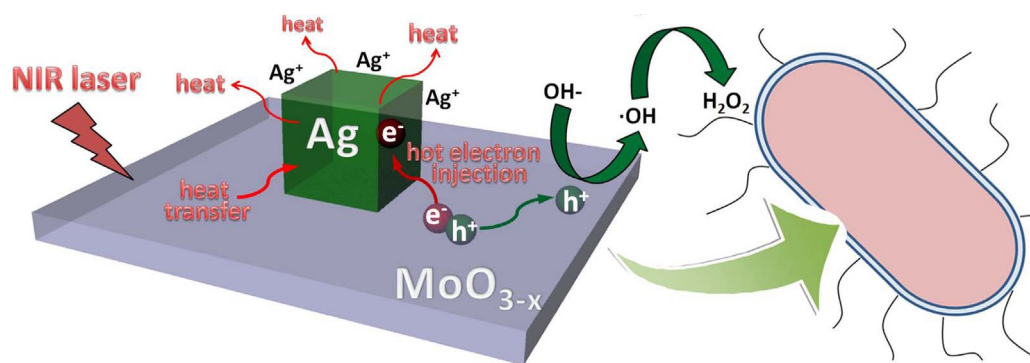


Fig. 8. Schematic illustration of the photocatalytic antibacterial mechanism of $\text{MoO}_{3-x}\text{-Ag}$ under NIR laser irradiation.

photothermal effect and silver release, $\text{MoO}_{3-x}\text{-Ag}$ only realizes the enhancement in comparison with bare MoO_{3-x} and Ag, respectively. In contrast, $\text{MoO}_{3-x}\text{-Ag}$ realizes the photocatalytic activity that MoO_{3-x} and Ag can not realize.

4. Conclusions

In summary, we demonstrated for the first time that plasmonic $\text{MoO}_{3-x}\text{-Ag}$ hybrid nanostructures were designed as high-efficient NIR antibacterial agent for killing pathogenic bacteria, in which Ag nanocubes were deposited on the flat surface of MoO_{3-x} nanosheets through face-to-face contact. Firstly, with the irradiation of $\text{MoO}_{3-x}\text{-Ag}$ with NIR laser, the excitation of plasmonic MoO_{3-x} nanosheets generates heat through photothermal effect, which helps to kill bacteria. Secondly, the photothermal effect produced heat diffuses to Ag nanocubes through the $\text{MoO}_{3-x}\text{-Ag}$ interface, which also triggers the release of Ag^+ and leads to the death of bacterial cells. Thirdly, NIR light excitation of MoO_{3-x} also produces hot charge carriers in the plasmonic MoO_{3-x} , and the hot electrons then transfer to Ag nanocubes through $\text{MoO}_{3-x}\text{-Ag}$ interface, while the separated hot holes left in the MoO_{3-x} act as major reactive species for the bacterial disinfection. Resulted from the synergic effect of plasmonic heating, Ag^+ release and free radical participating photocatalytic reaction, the designed $\text{MoO}_{3-x}\text{-Ag}$ exhibits superior removal efficiency towards both of *E. coli* and *S. aureus* in comparison with bare MoO_{3-x} and Ag under NIR laser irradiation. The advantage of the designed $\text{MoO}_{3-x}\text{-Ag}$ as antibacterial agent is also highlighted by the decreased cost and lowered toxicity of Ag nanocubes by MoO_{3-x} nanosheets.

Acknowledgements

This work is financially supported by the National Natural Science Foundation of China (No. 21603191, 21201151) and Zhejiang Provincial Natural Science Foundation of China (No. LQ16B010001, LY15B010003).

Appendix A. Supplementary data

Supplementary data associated with this article can be found, in the online version, at <http://dx.doi.org/10.1016/j.apcatb.2017.11.024>.

References

- [1] M.R. Hoffmann, S.T. Martin, W. Choi, D.W. Bahnemann, Environmental applications of semiconductor photocatalysis, *Chem. Rev.* 95 (1995) 69–96.
- [2] M.A. Shannon, P.W. Bohn, M. Elimelech, J.G. Georgiadis, B.J. Marinas, A.M. Mayes, Science and technology for water purification in the coming decades, *Nature* 452 (2008) 301–310.
- [3] M.M. Khin, A.S. Nair, V.J. Babu, R. Murugan, S. Ramakrishna, A review on nano-materials for environmental remediation, *Energy Environ. Sci.* 5 (2012) 8075–8109.
- [4] R. Fagan, D.E. McCormack, D.D. Dionysios, S.C. Pillai, A review of solar and visible light active TiO_2 photocatalysis for treating bacteria, cyanotoxins and contaminants of emerging concern, *Mater. Sci. Semicond. Process.* 42 (2016) 2–14.
- [5] W. He, H.K. Kim, W.G. Wamer, D. Melka, J.H. Callahan, Photogenerated charge carriers and reactive oxygen species in ZnO/Au hybrid nanostructures with enhanced photocatalytic and antibacterial activity, *J. Am. Chem. Soc.* 136 (2014) 750–757.
- [6] H. Kong, J. Song, J. Jiang, Photocatalytic antibacterial capabilities of TiO_2 -biocidal polymer nanocomposites synthesized by a surface-initiated photopolymerization, *Environ. Sci. Technol.* 44 (2010) 5672–5676.
- [7] Z. Yi, J. Ye, N. Kikugawa, T. Kako, S. Ouyang, H. Stuart-Williams, H. Yang, J. Cao, W. Luo, Z. Li, Y. Liu, R.L. Withers, An orthophosphate semiconductor with photo-oxidation properties under visible-light irradiation, *Nat. Mater.* 9 (2010) 559–564.
- [8] S. Bai, J. Jiang, Q. Zhang, Y. Xiong, Steering charge kinetics in photocatalysis: intersection of materials syntheses, characterization techniques and theoretical simulations, *Chem. Soc. Rev.* 44 (2015) 2893–2939.
- [9] H. Tong, S. Ouyang, Y. Bi, N. Umezawa, M. Oshikiri, J. Ye, Nano-photocatalytic materials: possibilities and challenges, *Adv. Mater.* 24 (2012) 229–251.
- [10] Z. Guo, S. Park, J. Yoon, I. Shin, Recent progress in the development of near-infrared fluorescent probes for bioimaging applications, *Chem. Soc. Rev.* 43 (2014) 16–29.
- [11] Y. Sang, H. Liu, A. Umar, Photocatalysis from UV/Vis to near-infrared light: towards full solar-light spectrum activity, *ChemCatChem* 7 (2015) 559–573.
- [12] W. Wang, Q. Shang, W. Zheng, H. Yu, X. Feng, Z. Wang, Y. Zhang, G. Li, A novel near-infrared antibacterial material depending on the upconverting property of $\text{Er}^{3+}\text{-Yb}^{3+}\text{-Fe}^{3+}$ tridoped TiO_2 nanopowder, *J. Phys. Chem. C* 114 (2010) 13663–13669.
- [13] L. Bai, W. Jiang, C. Gao, S. Zhong, L. Zhao, Z. Li, S. Bai, Facet engineered interface design of $\text{NaYF}_4\text{:Yb}$, Tm upconversion nanocrystals on BiOCl nanoplates for enhanced near-infrared photocatalysis, *Nanoscale* 8 (2016) 19014–19024.
- [14] Z. Zheng, T. Tachikawa, T. Majima, Single-particle study of Pt-modified Au nanorods for plasmon-enhanced hydrogen generation in visible to near-infrared region, *J. Am. Chem. Soc.* 136 (2014) 6870–6873.
- [15] W. Jiang, S. Bai, L. Wang, X. Wang, L. Yang, Y. Li, D. Liu, X. Wang, Z. Li, J. Jiang, Y. Xiong, Integration of multiple plasmonic and co-catalyst nanostructures on TiO_2 nanosheets for visible-near-infrared photocatalytic hydrogen evolution, *Small* 12 (2016) 1640–1648.
- [16] C. Fasciani, M.J. Silvero, M.A. Anghel, G.A. Arguello, M.C. Becerra, J.C. Scaiano, Aspartame-stabilized gold–silver bimetallic biocompatible nanostructures with plasmonic photothermal properties, antibacterial activity, and long-term stability, *J. Am. Chem. Soc.* 136 (2014) 17394–17397.
- [17] S. Mo, X. Chen, M. Chen, C. He, Y. Lu, N. Zheng, Two-dimensional antibacterial $\text{Pd}@\text{Ag}$ nanosheets with a synergetic effect of plasmonic heating and Ag^+ release, *J. Mater. Chem. B* 3 (2015) 6255–6260.
- [18] Y. Yang, T. Liu, L. Cheng, G. Song, Z. Liu, M. Chen, MoS_2 -based nanoprobes for detection of silver ions in aqueous solutions and bacteria, *ACS Appl. Mater. Interfaces* 7 (2015) 7526–7533.
- [19] H. Cheng, T. Kamegawa, K. Mori, H. Yamashita, Surfactant-free nonaqueous synthesis of plasmonic molybdenum oxide nanosheets with enhanced catalytic activity for hydrogen generation from ammonia borane under visible light, *Angew. Chem. Int. Ed.* 53 (2014) 2910–2914.
- [20] K. Manthiram, A.P. Alivisatos, Tunable localized surface plasmon resonances in tungsten oxide nanocrystals, *J. Am. Chem. Soc.* 134 (2012) 3995–3998.
- [21] G. Song, J. Shen, F. Jiang, R. Hu, W. Li, L. An, R. Zou, Z. Chen, Z. Qin, J. Hu, Hydrophilic molybdenum oxide nanomaterials with controlled morphology and strong plasmonic absorption for photothermal ablation of cancer cells, *ACS Appl. Mater. Interfaces* 6 (2014) 3915–3922.
- [22] B. Li, R. Long, X. Zhong, Y. Bai, Z. Zhu, X. Zhang, M. Zhi, J. He, C. Wang, Z.Y. Li, Y. Xiong, Investigation of size-dependent plasmonic and catalytic properties of metallic nanocrystals enabled by size control with HCl oxidative etching, *Small* 8 (2012) 1710–1716.
- [23] W. Li, P.H.C. Camargo, L. Au, Q. Zhang, M. Rycenga, Y. Xia, Etching and dimerization: a simple and versatile route to dimers of silver nanospheres with a range of sizes, *Angew. Chem. Int. Ed.* 49 (2010) 164–168.
- [24] G. Eisenberg, Colorimetric determination of hydrogen peroxide, *Ind. Eng. Chem. Anal. Ed.* 15 (1943) 327–328.
- [25] H. Wang, J. Gao, T. Guo, R. Wang, L. Guo, Y. Liu, J. Li, Facile synthesis of AgBr nanoplates with exposed {111} facets and enhanced photocatalytic properties, *Chem. Commun.* 48 (2012) 275–277.

- [26] S. Bai, X. Li, Q. Kong, R. Long, C. Wang, J. Jiang, Y. Xiong, Toward enhanced photocatalytic oxygen evolution: synergetic utilization of plasmonic effect and schottky junction via interfacing facet selection, *Adv. Mater.* 27 (2015) 3444–3452.
- [27] S. Sarina, H.Y. Zhu, Q. Xiao, E. Jaatinen, J. Jia, Y. Huang, Z. Zheng, H. Wu, Viable photocatalysts under solar-spectrum irradiation: nonplasmonic metal nanoparticles, *Angew. Chem. Int. Ed.* 53 (2014) 2935–2940.
- [28] W.A. Jacoby, P.C. Maness, E.J. Wolfrum, D.M. Blake, J.A. Fennell, Mineralization of bacterial cell mass on a photocatalytic surface in air, *Environ. Sci. Technol.* 32 (1998) 2650–2653.
- [29] T. Bao, W. Yin, X. Zheng, X. Zhao, J. Yu, X. Dong, Y. Yong, F. Gao, L. Yan, Z. Gu, Y. Zhao, One-pot synthesis of PEGylated plasmonic $\text{MoO}_{3/2}$ hollow nanospheres for photoacoustic imaging guided chemo-photothermal combinational therapy of cancer, *Biomaterial* 76 (2016) 11–24.
- [30] W. Shao, X. Liu, H. Min, G. Dong, Q. Feng, S. Zuo, Preparation characterization, and antibacterial activity of silver nanoparticle-decorated graphene oxide nanocomposite, *ACS Appl. Mater. Interfaces* 7 (2015) 6966–6973.
- [31] J. Liu, R.H. Hurt, Ion release kinetics and particle persistence in aqueous nano-silver colloids, *Environ. Sci. Technol.* 44 (2010) 2169–2175.
- [32] S. Ma, S. Zhan, Y. Jia, Q. Zhou, Superior antibacterial activity of Fe_3O_4 - TiO_2 nanosheets under solar light, *ACS Appl. Mater. Interfaces* 7 (2015) 21875–21883.
- [33] H. Cheng, X. Qian, Y. Kuwahara, K. Mori, H. Yamashita, A plasmonic molybdenum oxide hybrid with reversible tunability for visible-light-enhanced catalytic reactions, *Adv. Mater.* 27 (2015) 4616–4621.
- [34] L. Bai, F. Ye, L. Li, J. Lu, S. Zhong, S. Bai, Facet engineered interface design of plasmonic metal and cocatalyst on BiOCl nanoplates for enhanced visible photocatalytic oxygen evolution, *Small* 13 (2017) 1701617.
- [35] S. Mubeen, J. Lee, N. Singh, S. Kramer, G.D. Stucky, M. Moskovits, An autonomous photosynthetic device in which all charge carriers derive from surface plasmons, *Nat. Nanotechnol.* 8 (2013) 247–251.
- [36] S. Wang, Y. Gao, S. Miao, T. Liu, L. Mu, R. Li, F. Fan, C. Li, Positioning the water oxidation reaction sites in plasmonic photocatalysts, *J. Am. Chem. Soc.* 139 (2017) 11771–11778.
- [37] T. Xu, L. Zhang, H. Cheng, Y. Zhu, Significantly enhanced photocatalytic performance of ZnO via graphene hybridization and the mechanism study, *Appl. Catal. B: Environ.* 101 (2011) 382–387.
- [38] C. Hu, T. Peng, X. Hu, Y. Nie, X. Zhou, J. Qiu, H. He, Plasmon-induced photo-degradation of toxic pollutants with $\text{Ag-AgI/Al}_2\text{O}_3$ under visible-light irradiation, *J. Am. Chem. Soc.* 132 (2010) 857–862.
- [39] P. Bilski, K. Reszka, M. Bilska, C.F. Chignell, Oxidation of the spin trap 5,5-dimethyl-1-pyrroline *N*-oxide by singlet oxygen in aqueous solution, *J. Am. Chem. Soc.* 118 (1996) 1330–1338.
- [40] Y. Cui, Z. Ding, P. Liu, M. Antonietti, X. Fu, X. Wang, Metal-free activation of H_2O_2 by $\text{g-C}_3\text{N}_4$ under visible light irradiation for the degradation of organic pollutants, *Phys. Chem. Chem. Phys.* 14 (2012) 1455–1462.
- [41] L. Sun, Y. Qin, Q. Cao, B. Hu, Z. Huang, L. Ye, X. Tang, Novel photocatalytic antibacterial activity of TiO_2 microspheres exposing 100% reactive {111} facets, *Chem. Commun.* 47 (2011) 12628–12630.
- [42] L. Zhang, W. Wang, G. T. An, H.Y. Yip Li, Comparative study of visible-light-driven photocatalytic mechanisms of dye decolorization and bacterial disinfection by B^*Ni -codoped TiO_2 microspheres: the role of different reactive species, *Appl. Catal. B: Environ.* 108–109 (2011) 108–116.